

An extended Mori–Tanaka model for the elastic moduli of porous materials of finite size

S. Gong^{a,b}, Z. Li^{a,b,*}, Y.Y. Zhao^c

^a School of Materials Science and Engineering, Central South University, Changsha 410083, People's Republic of China

^b Key Laboratory of Nonferrous Metal Materials Science and Engineering, Ministry of Education, Changsha 410083, People's Republic of China

^c School of Engineering, University of Liverpool, Brownlow Hill, Liverpool L69 3GH, UK

Received 24 May 2011; received in revised form 16 July 2011; accepted 17 July 2011

Available online 8 August 2011

Abstract

The stepped equivalent substitution approach has been applied to extend the Mori–Tanaka model for predicting the elastic behavior of porous materials. A semi-infinite domain mechanics model has been developed to determine the Eshelby's tensors of the surface regions. The extended Mori–Tanaka model takes into account the effects of pore size, pore number and sample size. The model shows that: the elastic modulus of porous materials decreases with increasing porosity, with increasing number of pores, and with increasing difference between the pore sizes; the elastic modulus of porous materials is reduced when the ratio of sample diameter to average pore size is less than 20; micropores in excess of 5% can reduce the anisotropy of the elastic behavior in porous materials with oriented oblate spheroid macropores. The predicted elastic modulus values are in good agreement with the experimental data for a porous CuAlMn shape memory alloy containing oriented oblate spheroid pores of different specimen size, porosity (25–70%) and pore size, manufactured by the sintering–evaporation process.

© 2011 Acta Materialia Inc. Published by Elsevier Ltd. All rights reserved.

Keywords: Porous materials; Elastic modulus; Specimen size; Sintering–evaporation process

1. Introduction

Porous materials have attracted considerable attention in both academia and industry, mainly due to their exceptional mechanical properties, including energy absorption and sound absorption capabilities [1–4]. As the properties of porous materials depend to a large extent on the porosity and internal pore structure various models [5–7] have been developed to predict the structure-dependent mechanical performance of porous materials. Analytical models based on idealized or simplified conditions can often provide a useful tool to estimate the overall material

response. For example, Gibson and Ashby [1] obtained simple scaling equations on mechanical properties by modeling cell walls as beams and plates.

The Mori–Tanaka (MT) model [8,9] is one of the best known analytical approaches to determine the effective material constants of composite materials using homogenization techniques. It determines the Eshelby tensors using Eshelby's equivalent inclusion theory [10] and applies the homogenization technique to determine the properties of the composite material. Applications of this approach to the mechanical behavior of composite materials have been reported by Weng [11], Tandon and Weng [12] and Zhao et al. [13]. It has also been applied to model the thermal stresses and plastic deformation in metal matrix composites [14], damage development in polymer matrix short fibre composites [15] and many other properties, such as viscosity [16] and piezoelectricity [17].

* Corresponding author at: School of Materials Science and Engineering, Central South University, Changsha 410083, People's Republic of China. Tel.: +86 731 88830264; fax: +86 731 88876692.

E-mail addresses: lizhou6931@gmail.com, lizhou6931@163.com (Z. Li).

The MT model, however, has two main limitations: (a) the model is only suitable for composites with low volume fractions of inclusions; (b) the microstructure is assumed to be homogeneous, ignoring the effects of size and number of inclusions. In addition to these two limitations, application of the continuum MT model to small samples of porous materials can lead to significant errors because of the low ratios between sample size and cell size.

In this study the MT model was extended using a stepped equivalent substitution (SES) approach to calculate the elastic constants of porous materials containing different quantities of pores of different sizes. The effect of specimen size was studied using a semi-infinite domain mechanics model to determine the Eshelby's tensors of the surface regions. Validation of the extended MT (Ex-MT) model was conducted by comparing model predictions, first, with experimental data on the Young's modulus of porous metal specimens containing directional oblate spheroid pores with different porosities (25–70%), pore sizes and specimen sizes, fabricated by the sintering–evaporation process (SEP) [18], and then with experimental data on the Young's and shear moduli of some porous materials in the literature.

2. Model formulation

For brevity, symbolic notations will be used wherever appropriate. Greek letters denote the second rank tensors and ordinary capital letters denote the fourth rank ones. The inner product of two tensors is written such that $\sigma\varepsilon = \sigma_{ij}\varepsilon_{ij}$, $L\varepsilon = L_{ijkl}\varepsilon_{kl}$ and $LA = L_{ijkl}A_{klmn}$, in terms of the indicial components.

2.1. The Mori–Tanaka model

Consider an infinite composite material subject to a uniform stress σ^0 . The stress field of a monolithic material that has the same elastic behavior as the composite material, subject to the same uniform stress σ^0 , can be described by:

$$\sigma^0 = L^e \varepsilon^0,$$

where σ^0 is the stress tensor, ε^0 is the strain tensor and L^e is the stiff matrix of the monolithic material. L^e can be regarded as an equivalent stiff matrix of the composite material.

A composite material containing inclusions (or pores) is an Eshelby's inhomogeneous inclusion problem and the total stress field is given by [8]:

$$\sigma^0 + \tilde{\sigma} + \sigma' = L^p(\varepsilon^0 + \tilde{\varepsilon} + \varepsilon') = L^m(\varepsilon^0 + \tilde{\varepsilon} + \varepsilon' - \varepsilon^*), \quad (1)$$

where L^p is the stiff matrix of inclusions or pores, $\tilde{\sigma}$ is the average stress disturbance in the matrix due to the pores, $\tilde{\varepsilon}$ is the average strain disturbance in the matrix produced by $\tilde{\sigma}$, σ' and ε' are the stress disturbance and strain disturbance due to the existence of pores, respectively, and ε^* is Eshelby's equivalent “stress-free” strain for the pores.

From Eshelby [10] the strain disturbance is related to ε^* as:

$$\varepsilon' = S\varepsilon^*, \quad (2)$$

where S is Eshelby's tensor for pores, which depends on the matrix stiffness L^m and the shape of the pores. The requirement that the integration of the stress disturbance over the entire body vanishes leads to:

$$\tilde{\varepsilon} = -C(\varepsilon' - \varepsilon^*) = -C(S - I)\varepsilon^*, \quad (3)$$

where I is the fourth rank identity tensor and C is the volume fraction of the pores, i.e. porosity.

Given $L^p = 0$ (due to the pore), substituting Eqs. (2) and (3) into Eq. (1) provides a solution for ε^* :

$$\begin{aligned} \varepsilon^* &= A\varepsilon^0 \\ A &= \{L^m - L^m[CI + (1 - C)S]\}^{-1}L^m. \end{aligned} \quad (4)$$

The equivalent stiff matrix for the porous solid L^e is therefore:

$$L^e = L^m(I + CA)^{-1}, \quad (5)$$

which is an explicit expression and can be solved relatively easily.

2.2. The extended MT model

In the MT model the effect of the interactions between inclusions is underestimated. The SES approach, which transfers the interactions among inclusions (pores) to the interaction between an equivalent medium and an inclusion in a stepped manner, is introduced to solve this problem. Fig. 1 shows schematic diagrams of the Ex-MT model using the SES approach. In MT a stiff matrix L^m containing pores with volume fraction C is converted into a solid medium. The stiff matrix of the equivalent medium L^e is equal to that of the porous material. In Ex-MT pores are divided into several groups according to the shape, volume, orientation and even position. If the volume fraction of each group is equal and low enough then the effect of the interactions between pores can be ignored ($\lim_{C \rightarrow 0} \tilde{\varepsilon} = \lim_{C \rightarrow 0} -C(S - I)A\varepsilon^0 = 0$).

The matrix with the first group pores is converted into an equivalent medium by the MT model, the stiff matrix of which is L^1 . This equivalent medium is taken as a new matrix and combined with the remaining pores to form a new porous material (Fig. 1b). Applying the MT model again leads to another equivalent medium with a stiff matrix L^2 . The interactions between the first two groups of pores are calculated after substituting the first equivalent medium and forming the second new porous material (Fig. 1c). By repeating this process the interactions among all pores are considered and a final equivalent medium (Fig. 1d) is obtained. The stiff matrix of the final equivalent medium is considered to be the stiff matrix of the whole porous material, L^e . Since the equivalent medium for a matrix containing spheroid pores

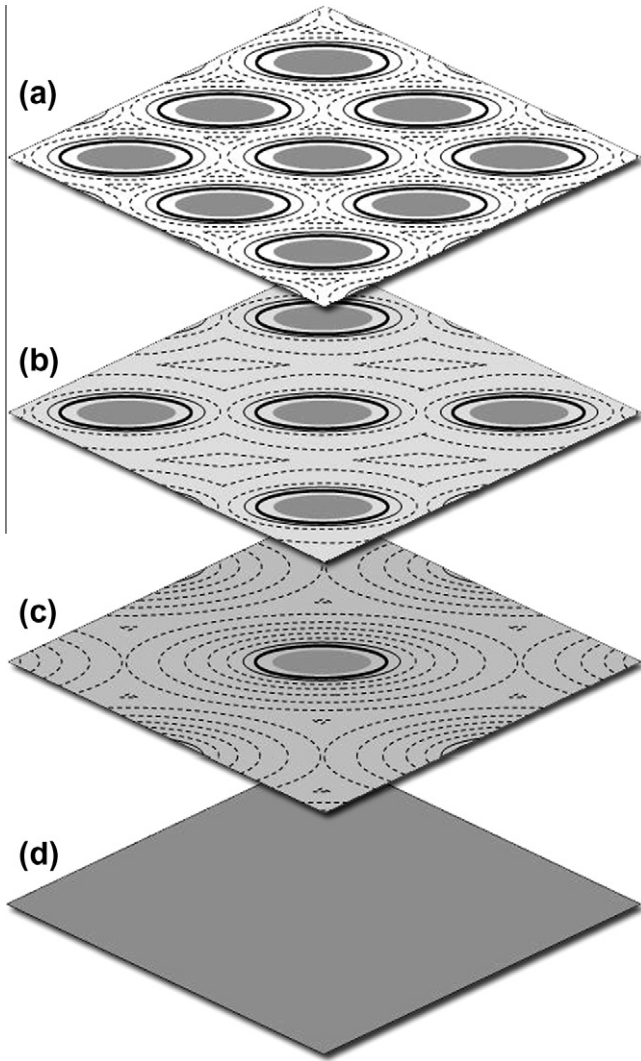


Fig. 1. Schematic diagram of the Ex-MT model using the stepped equivalent substitution approach. (a–d) Contour plots of the stress distribution for orientated oblate ellipsoid pores in the initial matrix, the first equivalent medium, the second equivalent medium, and the third equivalent medium, respectively. The stiff matrix of the final equivalent medium is considered to be the stiff matrix of the whole porous material.

is transversely isotropic, Eshelby's tensor for spheroid inclusions in a transversely isotropic matrix [19] is used, which is given in Appendix A.

It should be noted that the volume fraction of pores to calculate the equivalent medium is different from the volume fraction in the initial matrix. The volume fraction of the i th group of pores C_i is related to its real volume fraction, as well as the preceding pores in the initial matrix, by

$$C_i = \frac{C/n}{1 - C + (i \times C/n)}, \quad (6)$$

where n is the group numbers and C is the volume fraction of all pores in the initial matrix. Numerical calculations for the stiff matrix of a porous material containing pores using the SES approach were carried out using the MATLAB software. The stiff matrix of the first equivalent medium

was obtained using the stiff matrix of the initial matrix, $L^m = \lambda^m \delta_{ij} \delta_{kl} + \mu^m \delta_{ik} \delta_{jl} + \mu^m \delta_{il} \delta_{jk}$, and substituting Eqs. (4), (A1), and (6) into Eq. (5). λ^m and μ^m are the Lamé constants of the initial matrix, and δ_{ij} is the Kronecker delta. The equivalent flexibility matrix is therefore

$$M^e = (L^e)^{-1}.$$

For transversely isotropic materials M^e can be written as

$$\begin{bmatrix} M_{11}^e & M_{12}^e & M_{13}^e & 0 & 0 & 0 \\ M_{12}^e & M_{11}^e & M_{13}^e & 0 & 0 & 0 \\ M_{13}^e & M_{13}^e & M_{33}^e & 0 & 0 & 0 \\ 0 & 0 & 0 & M_{44}^e & 0 & 0 \\ 0 & 0 & 0 & 0 & M_{44}^e & 0 \\ 0 & 0 & 0 & 0 & 0 & 2(M_{11}^e - M_{12}^e) \end{bmatrix}.$$

The transverse effective modulus of the porous material E_{\parallel} is

$$E_{\parallel} = (M_{11}^e)^{-1}.$$

and the longitudinal effective modulus of the porous material E_{\perp} is

$$E_{\perp} = (M_{33}^e)^{-1}.$$

The Poisson ratios and the shear moduli can be obtained as

$$\begin{aligned} \nu_{12} &= -M_{12}^e/M_{11}^e, \nu_{31} = -M_{13}^e/M_{33}^e, \nu_{13} = -M_{13}^e/M_{11}^e, \\ G_{12} &= \frac{1}{2}(M_{11}^e - M_{12}^e), G_{13} = \frac{1}{2}(M_{11}^e - M_{13}^e). \end{aligned}$$

2.3. Eshelby tensor within the surface region

The Green function $G_{ij}(x, x')$ for a semi-infinite isotropic medium was obtained by Mindlin [20], and is given in Appendix B. Using $G_{ij}(x, x')$, the displacement $u_i(x)$ in the semi-finite domain as a result of the eigenstrain of the inclusion $\varepsilon_{mn}^*(x')$ can be expressed by [21]

$$U_i(x) = \int_0^{\infty} L_{jkmn}^m \varepsilon_{mn}^*(x') \frac{\partial}{\partial x'_k} G_{ij}(x, x') dx'. \quad (7)$$

Since the eigenstrain components satisfy ε_{33}^* , $\varepsilon_{11}^* = \varepsilon_{22}^*$, $\varepsilon_{12}^* = \varepsilon_{23}^* = \varepsilon_{31}^* = 0$ in uniform compression, the displacement is

$$\begin{aligned} u_i &= \frac{(\varepsilon_{33}^* - \varepsilon_{11}^*)}{8\pi(1-\nu)} \left[\psi_{,i33}^I - 2\nu\phi_{,i}^I - 4(1-\nu)\delta_{3i}\phi_{,i}^I + 2x_3\psi_{,i33}^{II} \right. \\ &\quad \left. + (3-4\nu)(1-2\delta_{3i})\psi_{,i33}^{II} - 2x_3^2\phi_{,i33}^{II} - 4(2-\nu)x_3\phi_{,i3}^{II} \right. \\ &\quad \left. + 4(1-2\nu)\delta_{3i}x_3\phi_{,i3}^{II} - 2(2-3\nu)\phi_{,i}^{II} + 4(3-4\nu)\delta_{3i}\phi_{,i}^{II} \right] \end{aligned}$$

The strain and stress components are, therefore:

$$\varepsilon_{ij} = \frac{1}{2}(u_{i,j} + u_{j,i}) = S_{ijkl} \varepsilon_{kl}^*,$$

$$\sigma_{ij} = L_{ijkl}^m (\varepsilon_{kl} - \varepsilon_{kl}^*),$$

where $\epsilon_{kl}^* = 0$ for the region outside the inclusion. The non-zero components of the stress tensor obtained by the above equation are given in Appendix C.

In the semi-infinite domain the stress field, within and without the inclusion, is a function of the shape of the inclusion and the distance of the inclusion from the surface. Fig. 2 shows the effects of c and the shape of the inclusion on the stress component at $x_1 = x_2 = x_3 = 0$. Fig. 2a1, b1 and c1, a2, b2 and c2 and a3, b3 and c3 show the cases with a free surface, without a surface, and the difference between the two, respectively. The stress component decreases with c in all cases and varies with the ratio of the eigenstrain $(-\epsilon_{33}^*/\epsilon_{11}^*)$. For a composite with pores as inclusions under uniaxial compression within the regime of elastic deformation $-\epsilon_{33}^*/\epsilon_{11}^*$ is the Poisson ratio ν_{31} of the porous material. The experiment results show that the Poisson ratio ν_{31} varies from 0.18 to 0.32, with an average value of 0.25. For each type of inclusion the existence of a surface leads to increased stress components at $x_1 = x_2 = x_3 = 0$ and the stress component decreases to zero at almost the same depth with or without the surface. Fig. 2a3, b3 and c3 is a good indicator of the effect of the free surface. For a spherical inclusion (Fig. 2a3) σ_{11} becomes almost 0 when

$c > 3a$. For the ellipsoid inclusion ($a_1 = a_2 = 3a_3$) with the major axis parallel to the free surface (Fig. 2b3) the stress component decreases to 0 after $c > 6a_3$. For the ellipsoid inclusion ($a_1 = a_2 = 3a_3$) with the major axis perpendicular to the free surface (Fig. 2c3) the stress component decreases to 0 after $c > 2a_1 = 6a_3$. In brief, the depth of the free surface effect changes with the shape of the inclusion but is not affected by the orientation of the inclusion. However, the value of the stress component is different with different inclusion orientations, even at the same depth.

The distribution of the stress component inside the inclusion can be obtained from Eq. (C1). Effected by a free surface the stress inside the ellipsoid inclusion is not constant but varies continuously and approximately linearly under a uniform eigenstrain ($\epsilon_{33}^*, \epsilon_{11}^* = \epsilon_{22}^*, \epsilon_{12}^* = \epsilon_{23}^* = \epsilon_{31}^* = 0$). The average stress component ϵ inside the inclusion can be substituted by the stress component at the geometrical center ($x_1 = x_2 = 0, x_3 = c$) of the ellipsoid inclusion. Fig. 3 shows the stress distribution inside the inclusion when $c = 2a_3$. Fig. 4 shows the variation of the stress component inside the ellipsoid inclusion at $x_1 = x_2 = 0, x_3 = c$ with c due to the effect of the free surface.

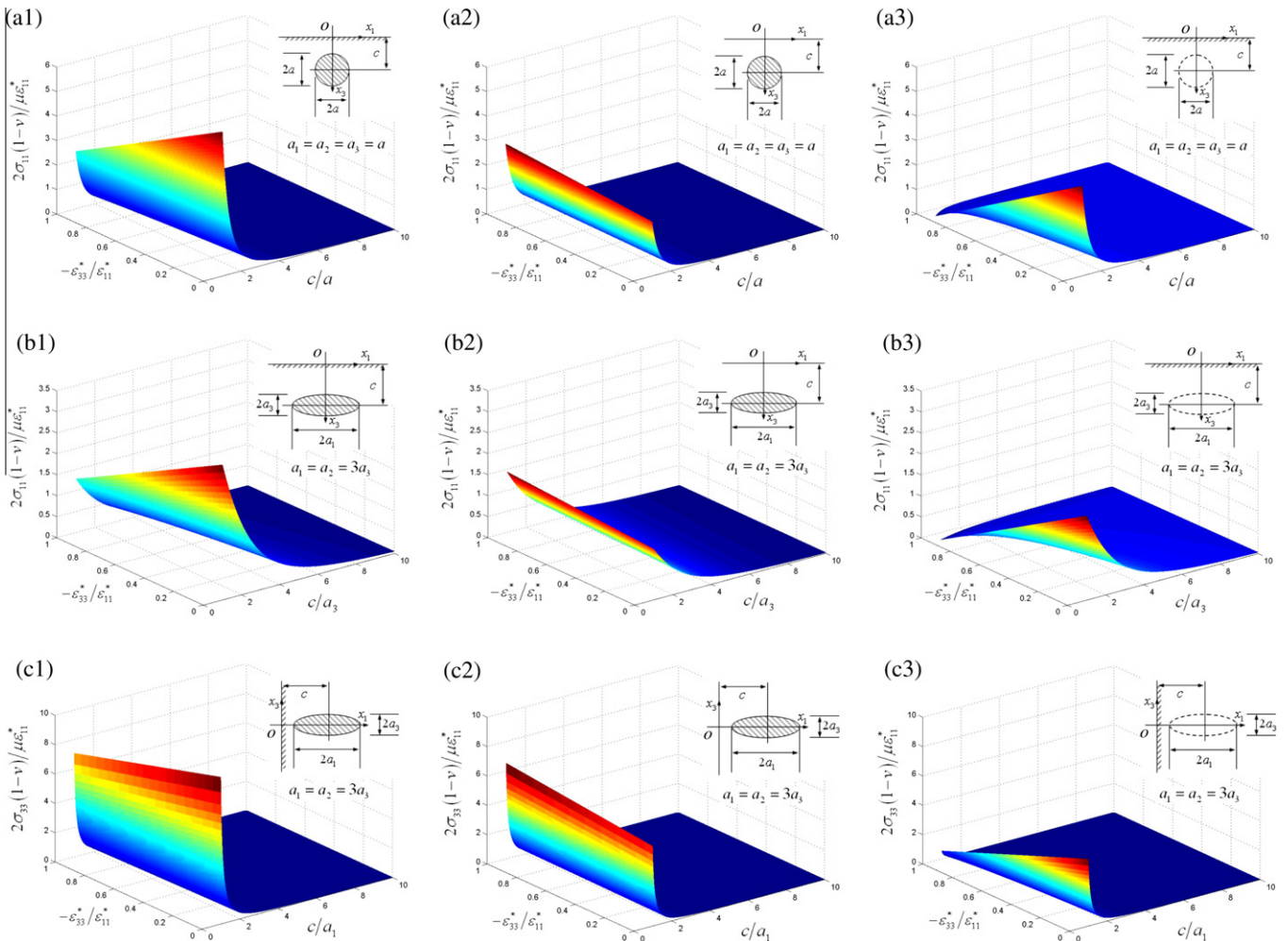


Fig. 2. The stress component at $x_1 = x_2 = x_3 = 0$ showing the effects of c and the shapes of the inclusions.

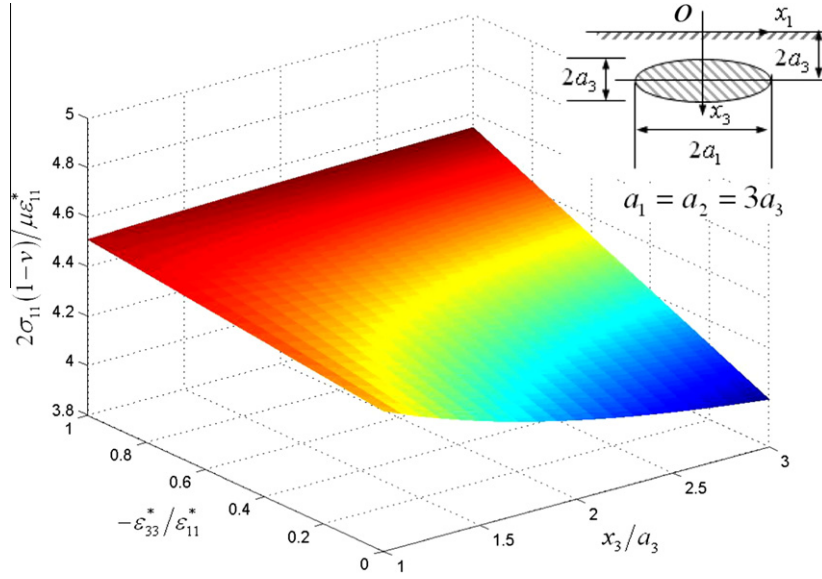


Fig. 3. Stress distribution inside the inclusion when $c = 2a_3$.

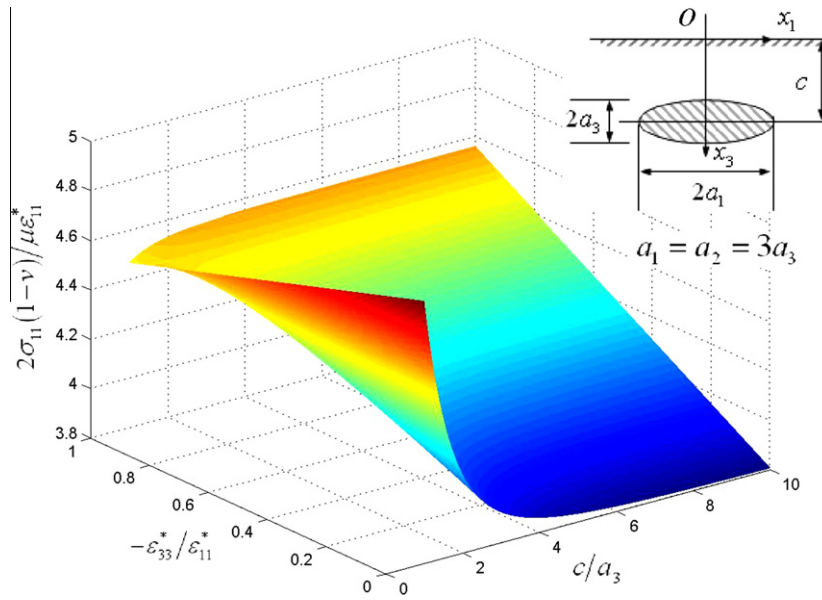


Fig. 4. Variation of the stress component inside the ellipsoid inclusion at $x_1 = x_2 = 0$, $x_3 = c$ with c due to the effect of the free surface.

The depth of the effect area is taken as the critical depth of inclusion c_c when the stress at the surface approximates 0. For a spherical inclusion with radius $a_c = 3a$, and for an ellipsoid inclusion $a_1 = a_2 = 3a_3$, $c_c = 6a_3$, irrespective of whether the major or minor axis is parallel to the free surface. The average stress components $\hat{\sigma}$ within the effect area and the corresponding average strain components $\hat{\varepsilon}$ can be calculated as

$$\hat{\sigma}_{11} = \frac{\int_{a_p}^{c_c} \sigma_{11}(c) dc}{c_c - a_p}, \quad \hat{\sigma}_{33} = \frac{\int_{a_p}^{c_c} \sigma_{33}(c) dc}{c_c - a_p},$$

$$\hat{\varepsilon}_{11} = \frac{\int_{a_p}^{c_c} \hat{\varepsilon}_{11}(c) dc}{c_c - a_p}, \quad \hat{\varepsilon}_{33} = \frac{\int_{a_p}^{c_c} \hat{\varepsilon}_{33}(c) dc}{c_c - a_p},$$

where a_p is the radius of inclusion perpendicular to the free surface. The average Eshelby's tensor within the surface effect area is

$$\hat{S}_{ijkl} = \hat{\varepsilon}_{ij} / \hat{\varepsilon}_{kl}^* \quad (8)$$

This tensor can be used to calculate the equivalent stiff matrix containing the surface effect area using the Ex-MT approach.

3. Evaluation and discussion

3.1. Porous materials for evaluation

The porous materials used to evaluate the validity of the Ex-MT model are porous CuAlMn SMA samples

manufactured by SEP [18,22–26]. Fig. 5 shows outline of the fabrication strategy for porous metals with oriented oblate ellipsoid pores. The raw materials used were Cu–11.9Al–2.5Mn (wt.%) alloy and NaCl powders. The particles of the CuAlMn powder were nearly spherical and had smooth surfaces with sizes less than 75 μm . Two NaCl powders (99.0% purity) having flake-like particles with sizes in the range 355–800 and 800–1000 μm , respectively, were used. The CuAlMn and NaCl powders were mixed at weight ratios of 3:2, 2:1, 3:1, 4:1, 6:1 and 10:1. A small amount of ethanol, ~ 0.5 vol.% of the powder mixture, was added as a binder during mixing. The powder mixture was poured into a high strength graphite die and placed in a vacuum furnace for hot press sintering. The mixture was first heated to 200 $^{\circ}\text{C}$ to evaporate the ethanol and then heated to 780 $^{\circ}\text{C}$ and hot pressed at a pressure of 28 MPa for 3 h under a vacuum of 0.01 Pa. After plunger was removed the sample was further heated to 930 $^{\circ}\text{C}$ for 6 h to melt and evaporate the NaCl (the melting points of NaCl and CuAlMn are 801 $^{\circ}\text{C}$ and 1040 $^{\circ}\text{C}$, respectively), followed by cooling to room temperature. The dimensions of the samples were 24 \times 10 \times 10 mm, 12 \times 5 \times 5 mm or 6 \times 2.5 \times 2.5 mm. All the samples were subjected to solution treatment at 850 $^{\circ}\text{C}$ for 20 min followed by water quenching, leading to a martensitic structure.

The pore characteristics of the porous samples were observed using scanning electron microscopy (FEI Siron200). In longitudinal sections the ellipsoidal pores are oriented, with the major axis perpendicular to and the minor axis parallel to the direction of the pressure applied during hot press sintering. The orientation of the pores is a result of rearrangement of the flake-like NaCl particles under pressure. The porosity of a sample was obtained by measuring the density and comparing it with the density of the bulk alloy (7.5 kg m^{-3}). The elastic moduli of the samples were measured by uniaxial compression at room

temperature according to ASTM standard E-9. The elastic properties of the bulk CuAlMn SMA were measured as $E_0 = 11.63$ GPa and $\nu_0 = 0.33$, which are regarded as the properties of the matrix in this paper.

3.2. Results and discussion

In MT only the volume fraction, shape and orientation of the inclusions are considered. The equivalent elastic behavior of a composite is considered to be independent of the size and number of inclusions. In practice there exists an interaction between the stress fields of the inclusions, which varies with the relative sizes and relative positions of the inclusions. This interaction influences the elastic behavior of the composite. The influence cannot be ignored, especially when there is a great difference in elastic behavior between the inclusions and the matrix (e.g. porous metals).

In Ex-MT pores are divided into several groups and the number of groups (n) must be more than enough to ensure that the volume fraction of each group is low. Fig. 6 shows the normalized elastic moduli of porous materials with different group numbers of pores, calculated using the Ex-MT model. When $n = 1$ there is only one type of pore in the matrix and the Ex-MT and MT models produce the same results. In the other cases the elastic moduli of the porous materials are reduced because of interactions between the pores. The elastic moduli of porous materials are almost the same when the group number of pores is greater than 20. In this case the interactions among pores are drivers for stabilization and the pore groups in the Ex-MT model are just sufficient. Fig. 6b shows that the anisotropy of the pore structure results in anisotropy of the elastic behavior. The elastic modulus in the transverse direction is always lower than that in the longitudinal direction and the interactions of pores is more pronounced in the transverse

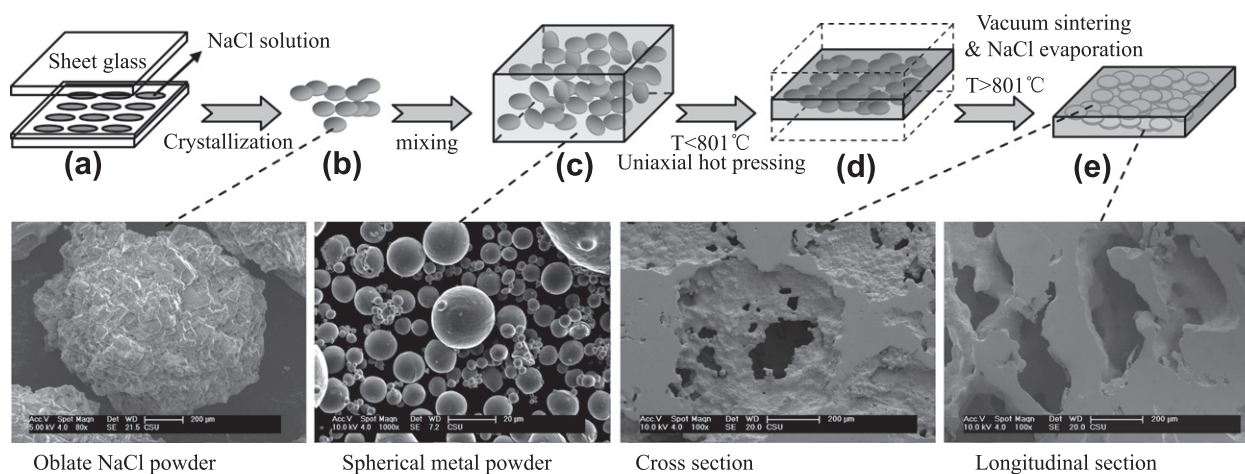


Fig. 5. Outline of the fabrication strategy for porous metals with oriented oblate ellipsoid pores. (a) Hollowed out sheet glass sandwich with NaCl saturated solution. (b) The prepared NaCl powder with an oblate ellipsoid shape. (c) The mixture of NaCl powders and spherical metal powders (prepared by a liquid spraying process). (d) Rearrangement of the oblate NaCl particles under uniaxial pressure (the melting point of NaCl is 801 $^{\circ}\text{C}$). (e) The final porous metals with oriented oblate ellipsoid pores (the space hold NaCl was completely eliminated during vacuum sintering at high temperature and strong metallurgical bonding in the cell walls was achieved).

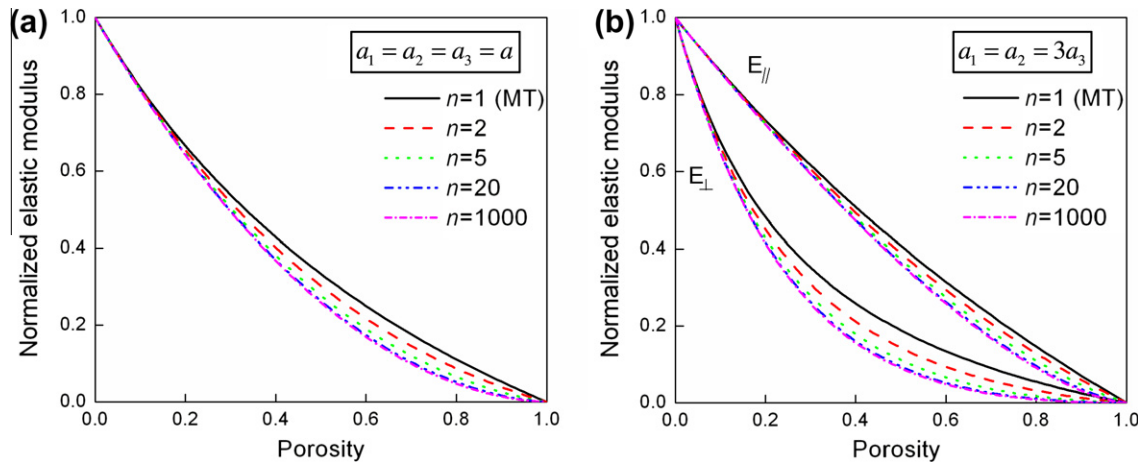


Fig. 6. Normalized elastic moduli of porous materials with (a) spherical and (b) oriented oblate ellipsoid pores, calculated using the Ex-MT model and the SHS approach (n is the number of pore groups).

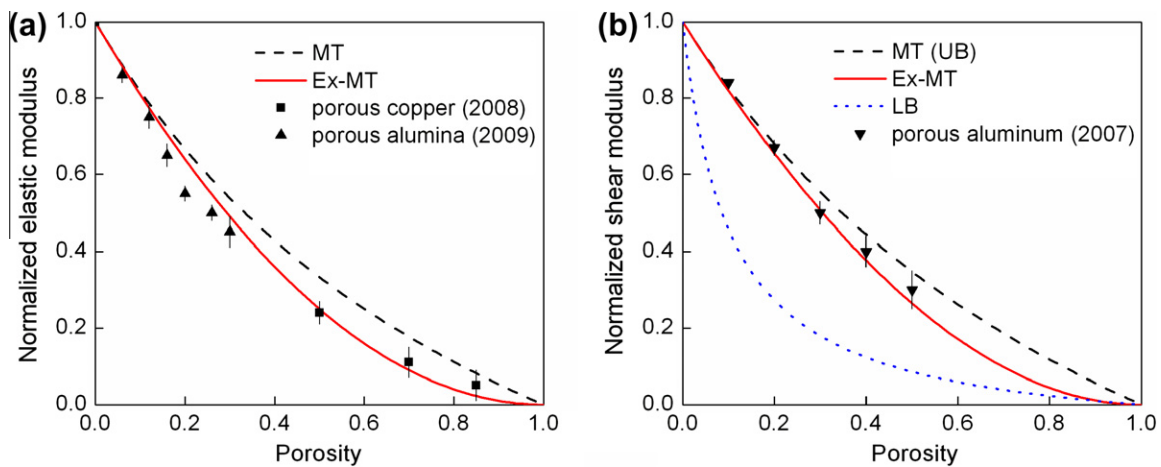


Fig. 7. Variations in normalized elastic modulus and shear modulus with porosity for porous materials with spherical pores.

direction. Fig. 7 compares the normalized elastic modulus and shear modulus of porous materials with spherical pores as a function of porosity between experimental values reported in the literature [27–29] and the MT and Ex-MT model predictions. The theoretical upper (UB) and lower (LB) bounds for the shear modulus given by Hashin and Shtrikman [30] are also shown. The values calculated from Ex-MT ($n = 20$) are in good agreement with the experimental values, while the values obtained from MT are always higher than those from Ex-MT.

In order to study the effect of surface region and sample size on the stiff matrix of porous materials the Ex-MT model was applied to a series of samples with different sample–pore size ratios. Fig. 8 shows schematic diagrams of typical samples containing oriented ellipsoid pores. The actual surface of the samples is usually not flat, because the ellipsoid pores at the surface would be cut open during machining. Before applying the Ex-MT model the actual surface is substituted by an equivalent flat surface which will not change the total porosity of the specimen.

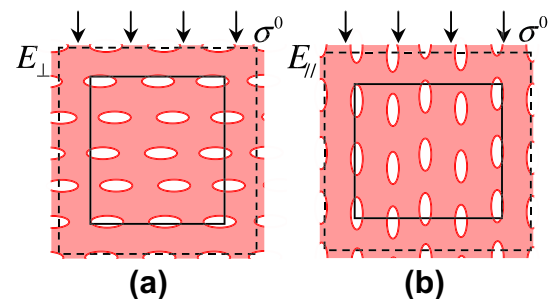


Fig. 8. Schematic diagrams of typical samples containing oriented ellipsoid pores. The arrows indicate the deformation direction, the dashed line represents the equivalent free surface, and the area outside the solid line represents the surface effect area.

The equivalent free surface is represented by the dashed line. The surface effect area is represented by the area between the solid and dashed lines.

Fig. 9 shows the normalized elastic moduli of the porous material parallel and perpendicular to the major axis of the

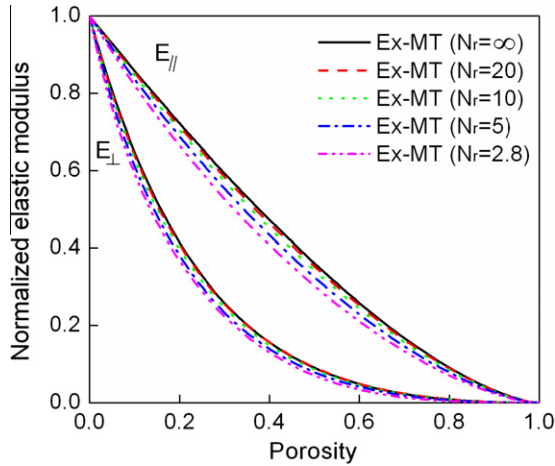


Fig. 9. Effect of sample pore size ratio on the porosity-dependent normalized elastic moduli of the porous material parallel (E_{\parallel}) and perpendicular (E_{\perp}) to the major axis of the oblate spheroid pores.

oblate spheroid pores as a function of porosity at different size ratios, calculated using the Ex-MT model. The size ratio N_r is defined as the ratio between the diameter of the cylindrical specimen or the width of the rectangular specimen and the average pore size. It is shown that the size

ratio has an influence on the elastic moduli of the porous material, with lower size ratios leading to lower moduli. The results are consistent with the experimental evidence provided by Lakes [31] and Brezny and Green [32] that porous materials can be treated as a continuum only if the diameter of the test specimens is greater than 20 times the cell size.

The calculated and measured elastic moduli values of the porous CuAlMn SMA with different N_r values are shown in Fig. 10. The dashed lines show the values calculated by the MT model, i.e. without considering the effect of specimen size. The solid lines show the values calculated by the Ex-MT model, which considers the surface effect. The Ex-MT model predictions are in very good agreement with the experimental values, while the MT model over-predicted the elastic modulus values in both the parallel and perpendicular directions. In some cases the Ex-MT model can be approximated by simple expressions. Table 1 shows the approximate expressions for the normalized elastic moduli of porous materials with a few typical pore shapes and sample-pore ratios.

Porous materials fabricated by space holder techniques have macropores resulting from the space holder particles and micropores on the pore walls. The micropores are

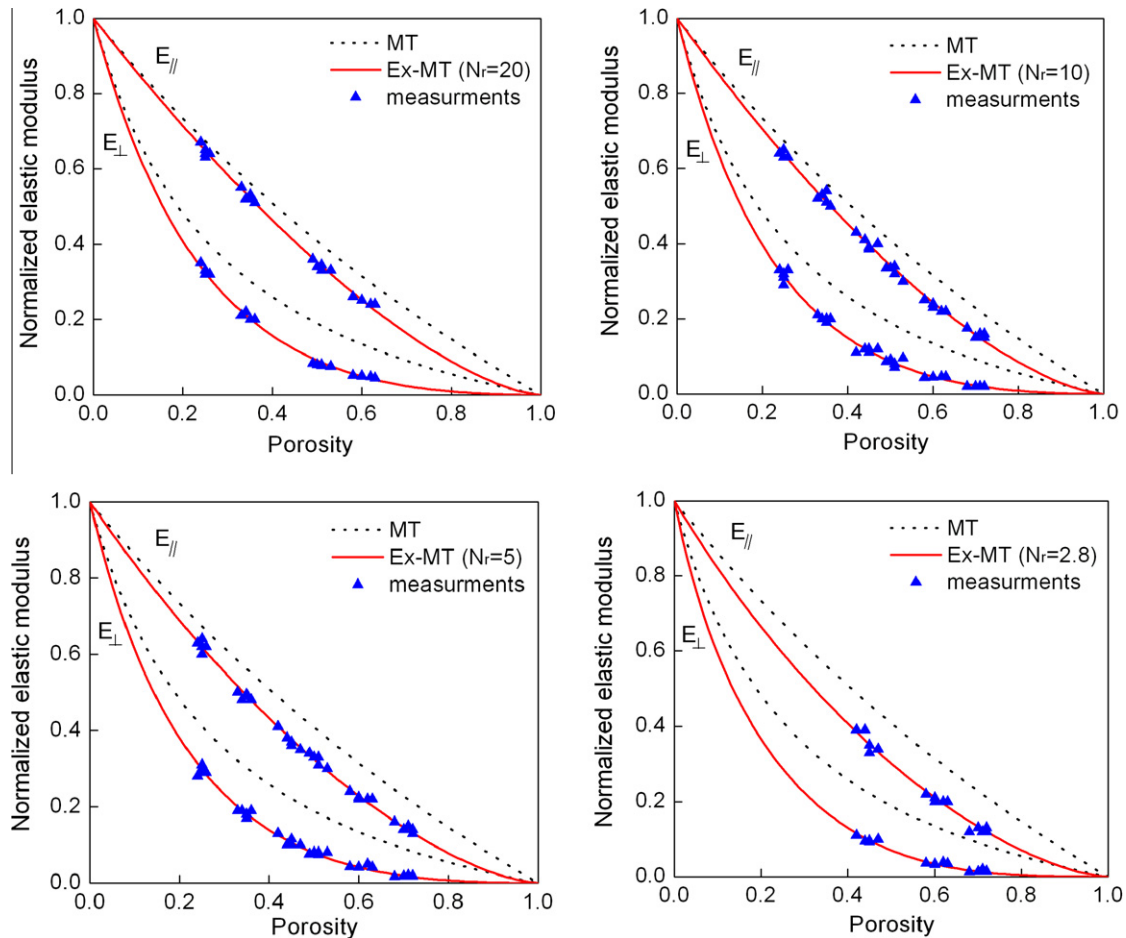


Fig. 10. The calculated and measured elastic moduli values of the porous CuAlMn SMA with different N_r values.

Table 1

Approximate expressions for the normalized elastic moduli of porous materials obtained from the Ex-MT model.

Pore shape	N_r	E_{\parallel}	E_{\perp}	Useful range
$a_1 = a_2 = a_3$	≥ 20	$(1-p)^2$	$(1-p)^2$	$p = 0-1$
$a_1 = a_2 = 3a_3$	≥ 20	$(1-p)^{1.5}$	$0.8 \times (1-p)^{3.15}$	$p = 0.25-0.75$
$a_1 = a_2 = 3a_3$	10	$(1-p)^{1.55}$	$0.8 \times (1-p)^{3.23}$	$p = 0.25-0.75$
$a_1 = a_2 = 3a_3$	5	$(1-p)^{1.61}$	$0.8 \times (1-p)^{3.4}$	$p = 0.25-0.75$
$a_1 = a_2 = 3a_3$	2.8	$(1-p)^{1.73}$	$0.8 \times (1-p)^{3.5}$	$p = 0.25-0.75$

p , porosity; a_1 , a_2 and a_3 , the radii of the oblate ellipsoid pores.

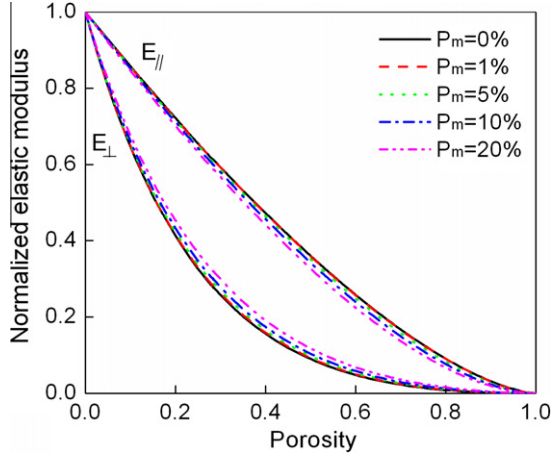


Fig. 11. The effect of spherical micropores on the elastic behavior of porous materials with oblate spheroid macropores ($a_1 = a_2 = 3a_3$).

often approximately spherical and are formed due to partial sintering of the metal powder matrix. Fig. 11 shows the effect of the spherical micropores on the elastic behavior of porous materials with oblate spheroid macropores. When the total porosity of the micropores P_m is less than 5% the effect of micropores can be ignored. When the porosity of the micropores is higher than 5% there are slight decreases in the elastic modulus in the parallel direction, accompanied by slight increases in the perpendicular direction. In other words, the existence of micropores mitigates the anisotropy of elastic behavior. In SEP the sintering temperature is high enough to achieve strong metallurgical bonding in the cell walls. The number of micropores is few and the total porosity of the micropores is less than 1%. The effect of micropores does not need to be considered in the modeling.

4. Conclusions

1. The Ex-MT model can predict the elastic behavior of porous materials and the effect on the specimen surface very well. The predicted elastic modulus values are in good agreement with the experimental values.
2. The depth of the surface effect area varies with the shape of the pores. For spherical pores it is equal to $3a$. For oblate spheroid pores ($a_1 = a_2 = 3a_3$) it is equal to $6a_3$.

3. The Ex-MT model confirms that the elastic modulus of porous materials is reduced when the ratio of specimen diameter to average pore size is less than 20.
4. Micropores in excess of 5% can reduce the anisotropy of the elastic behavior in porous materials with oriented oblate spheroid macropores.

Acknowledgement

This research work was supported by a Science and Technology Innovation Teams in Higher Education Institutions award by Hunan province.

Appendix A. Eshelby's tensor for spheroid inclusions in a transversely isotropic matrix

Lin and Mura [19] gave expressions for the elastic fields of oblate spheroid inclusions in a transversely isotropic matrix. The coordinates are assumed to be coincident with the principal directions of the spheroid inclusion, which is expressed by $(x_1^2/a_1^2) + (x_2^2/a_1^2) + (x_3^2/a_3^2) \leq 1$. The ratio a_1/a_3 is denoted by ρ and $\rho \geq 1$.

For a transversely isotropic matrix the elastic moduli are denoted by

$$\begin{aligned} L_{11}^m &= d, & \frac{1}{2}(L_{11}^m - L_{12}^m) &= e, & L_{44}^m &= f, & L_{13}^m + L_{44}^m \\ &= g, & L_{33}^m &= h, \end{aligned}$$

where L_{ij}^m are the Voigt constants. The non-zero components of \bar{G}_{ijkl} are given below:

$$\begin{aligned} \bar{G}_{1111} &= \bar{G}_{2222} = \frac{1}{2} \pi \int_0^1 \Delta(1-x^2) \{ [f(1-x^2) + h\rho^2x^2] \\ &\quad \times [(3e+d)(1-x^2) + 4f\rho^2x^2] - g^2\rho^2x^2(1-x^2) \} dx, \\ \bar{G}_{3333} &= 4\pi \int_0^1 \Delta\rho^2x^2 [d(1-x^2) + f\rho^2x^2] [e(1-x^2) + f\rho^2x^2] dx, \\ \bar{G}_{1122} &= \bar{G}_{2211} = \frac{1}{2} \pi \int_0^1 \Delta(1-x^2) \{ [f(1-x^2) + h\rho^2x^2] \\ &\quad \times [(e+3d)(1-x^2) + 4f\rho^2x^2] - 3g^2\rho^2x^2(1-x^2) \} dx, \\ \bar{G}_{1133} &= \bar{G}_{2233} = 2\pi \int_0^1 \Delta\rho^2x^2 \{ [(d+e)(1-x^2) + 2f\rho^2x^2] \\ &\quad \times [f(1-x^2) + h\rho^2x^2] - g^2\rho^2x^2(1-x^2) \} dx, \\ \bar{G}_{3311} &= \bar{G}_{3322} = 2\pi \int_0^1 \Delta(1-x^2) [d(1-x^2) + f\rho^2x^2] \\ &\quad \times [e(1-x^2) + f\rho^2x^2] dx, \\ \bar{G}_{1212} &= \frac{1}{2} \pi \int_0^1 \Delta(1-x^2)^2 \{ g^2\rho^2x^2 - (d-e)[f(1-x^2) \\ &\quad + h\rho^2x^2] \} dx, \\ \bar{G}_{1313} &= \bar{G}_{2323} \\ &= (-2\pi) \int_0^1 \Delta g\rho^2x^2(1-x^2) [e(1-x^2) + f\rho^2x^2] dx, \end{aligned}$$

where

$$A^{-1} = [e(1-x^2) + f\rho^2x^2] \{ [d(1-x^2) + f\rho^2x^2] \\ \times [f(1-x^2) + h\rho^2x^2] - g^2\rho^2x^2(1-x^2) \}.$$

The Eshelby's tensor S is calculated as [21]:

$$S_{ijmn} = \frac{1}{8\pi} L_{pqmn}^m (\bar{G}_{ipjq} + \bar{G}_{jpiq}). \quad (A1)$$

Appendix B. The Green tensor for a semi-infinite isotropic material

The Green tensor $G_{ij}(x, x')$ necessary for calculation of the displacement field in $x (x_1, x_2, x_3)$ induced by a point force applied at $x' (x'_1, x'_2, x'_3)$ was given by Mindlin [20], using $R_1 = [(x_1 - x'_1)^2 + (x_2 - x'_2)^2 + (x_3 - x'_3)^2]^{1/2}$, the distance between the two points, and $R_2 = [(x_1 - x'_1)^2 + (x_2 - x'_2)^2 + (x_3 + x'_3)^2]^{1/2}$, the distance between point $x (x_1, x_2, x_3)$ and the mirror image of point $x' (x'_1, x'_2, x'_3)$ through the surface located at $x_3 = 0$.

$$G_{ij}(x, x') = \frac{1}{16\pi\mu(1-\nu)} \left[\frac{3-4\nu}{R_1} \delta_{ij} + \frac{1}{R_2} \delta_{ij} + \frac{(x_i - x'_i)(x_j - x'_j)}{R_1^3} \right. \\ \left. + \frac{(3-4\nu)(x_i - x'_i)(x_j - x'_j)}{R_2^3} + \frac{2x_3x'_3}{R_2^3} \right. \\ \left. \times \left\{ \delta_{ij} - \frac{3(x_i - x'_i)(x_j - x'_j)}{R_2^2} \right\} \right. \\ \left. + \frac{4(1-\nu)(1-2\nu)}{R_2 + x_3 + x'_3} \right. \\ \left. \times \left\{ \delta_{ij} - \frac{(x_i - x'_i)(x_j - x'_j)}{R_2(R_2 + x_3 + x'_3)} \right\} \right] = G_{ji}(x, x'),$$

$$G_{3j}(x, x') = \frac{(x_j - x'_j)}{16\pi\mu(1-\nu)} \left[\frac{(x_3 - x'_3)}{R_1^3} + \frac{(3-4\nu)(x_3 - x'_3)}{R_2^3} \right. \\ \left. - \frac{6x_3x'_3(x_3 - x'_3)}{R_2^5} + \frac{4(1-\nu)(1-2\nu)}{R_2(R_2 + x_3 + x'_3)} \right],$$

$$G_{i3}(x, x') = \frac{(x_i - x'_i)}{16\pi\mu(1-\nu)} \left[\frac{(x_3 - x'_3)}{R_1^3} + \frac{(3-4\nu)(x_3 - x'_3)}{R_2^3} \right. \\ \left. + \frac{6x_3x'_3(x_3 - x'_3)}{R_2^5} - \frac{4(1-\nu)(1-2\nu)}{R_2(R_2 + x_3 + x'_3)} \right],$$

$$G_{33}(x, x') = \frac{1}{16\pi\mu(1-\nu)} \left[\frac{3-4\nu}{R_1} + \frac{8(1-\nu)^2 - (3-4\nu)}{R_2} \right. \\ \left. + \frac{(x_3 - x'_3)^2}{R_1^3} + \frac{(3-4\nu)(x_3 + x'_3)^2 - 2x_3x'_3}{R_2^3} \right. \\ \left. + \frac{6x_3x'_3(x_3 + x'_3)^2}{R_2^5} \right], \quad i, j = 1, 2, \quad (B1)$$

where μ is the shear modulus and ν is the Poisson ratio.

Appendix C. The non-zero components of the stress tensor

The non-zero components of the stress tensor are:

$$\sigma_{11} = \frac{\mu(\varepsilon_{33}^* - \varepsilon_{11}^*)}{4\pi(1-\nu)} \left[\psi_{,1133}^I + 2v\phi_{,22}^I + 2x_3\psi_{,11333}^I \right. \\ \left. + (3-4\nu)\psi_{,1133}^{II} - 4v\psi_{,3333}^{II} - 2x_3^2\phi_{,1133}^{II} - 4(2-\nu)x_3\phi_{,113}^{II} \right. \\ \left. + 4vx_3\phi_{,333}^{II} - 2(2-3v)\phi_{,11}^{II} + 14v\phi_{,33}^{II} \right] - \frac{(1+\nu)\mu\varepsilon_{11}^*}{2\pi(1-\nu)} \\ \times \left[\phi_{,11}^I + 2x_3\phi_{,113}^{II} + (3-4\nu)\phi_{,11}^{II} - 4v\phi_{,33}^{II} \right], \\ \sigma_{22} = \frac{\mu(\varepsilon_{33}^* - \varepsilon_{11}^*)}{4\pi(1-\nu)} \left[\psi_{,2233}^I + 2v\phi_{,11}^I + 2x_3\psi_{,22333}^{II} \right. \\ \left. + (3-4\nu)\psi_{,2233}^{II} - 4v\psi_{,3333}^{II} - 2x_3^2\phi_{,2233}^{II} - 4(2-\nu)x_3\phi_{,223}^{II} \right. \\ \left. + 4vx_3\phi_{,333}^{II} - 2(2-3v)\phi_{,22}^{II} + 14v\phi_{,33}^{II} \right] - \frac{(1+\nu)\mu\varepsilon_{11}^*}{2\pi(1-\nu)} \\ \times \left[\phi_{,22}^I + 2x_3\phi_{,223}^{II} + (3-4\nu)\phi_{,22}^{II} - 4v\phi_{,33}^{II} \right], \\ \sigma_{33} = \frac{\mu(\varepsilon_{33}^* - \varepsilon_{11}^*)}{4\pi(1-\nu)} \left[\psi_{,3333}^I - 4\phi_{,33}^I - \psi_{,3333}^{II} + 4\phi_{,33}^{II} \right. \\ \left. + 2x_3\psi_{,33333}^{II} - 2x_3^2\phi_{,3333}^{II} - 8x_3\phi_{,333}^{II} \right] \\ - \frac{(1+\nu)\mu\varepsilon_{11}^*}{2\pi(1-\nu)} \left[\phi_{,33}^I - \phi_{,33}^{II} + 2x_3\phi_{,333}^{II} \right], \\ \sigma_{12} = \frac{\mu(\varepsilon_{33}^* - \varepsilon_{11}^*)}{4\pi(1-\nu)} \left[\psi_{,1233}^I - 2v\phi_{,12}^I + 2x_3\psi_{,12333}^{II} + (3-4\nu)\psi_{,1233}^{II} \right. \\ \left. - 2x_3^2\phi_{,1233}^{II} - 4(2-\nu)x_3\phi_{,123}^{II} - 2(2-3v)\phi_{,12}^{II} \right] \\ \sigma_{23} = \frac{\mu(\varepsilon_{33}^* - \varepsilon_{11}^*)}{4\pi(1-\nu)} \left[\psi_{,2333}^I - 2v\phi_{,23}^I + 2x_3\psi_{,23333}^{II} + \psi_{,2333}^{II} \right. \\ \left. - 2x_3^2\phi_{,2333}^{II} - 8x_3\phi_{,233}^{II} - 2\phi_{,23}^{II} \right] \\ - \frac{(1+\nu)\mu\varepsilon_{11}^*}{2\pi(1-\nu)} \left[\phi_{,23}^I + 2x_3\phi_{,233}^{II} + \phi_{,23}^{II} \right], \\ \sigma_{31} = \frac{\mu(\varepsilon_{33}^* - \varepsilon_{11}^*)}{4\pi(1-\nu)} \left[\psi_{,1333}^I - 2v\phi_{,13}^I + 2x_3\psi_{,13333}^{II} + \psi_{,1333}^{II} \right. \\ \left. - 2x_3^2\phi_{,1333}^{II} - 8x_3\phi_{,133}^{II} - 2\phi_{,13}^{II} \right] - \frac{(1+\nu)\mu\varepsilon_{11}^*}{2\pi(1-\nu)} \\ \times \left[\phi_{,13}^I + 2x_3\phi_{,133}^{II} + \phi_{,13}^{II} \right]. \quad (C1)$$

where

$$\phi_{,i}^I = \frac{\partial}{\partial x_i}(\phi^I), \quad \phi_{,i}^{II} = \frac{\partial}{\partial x_i}(\phi^{II}), \\ \psi^I = \int_{\Omega} R_1 dx', \quad \phi^I = \int_{\Omega} \frac{1}{R_1} dx', \quad \psi^{II} = \int_{\Omega} R_2 dx', \\ \phi^{II} = \int_{\Omega} \frac{1}{R_2} dx'.$$

The domain of integration Ω is

$$\frac{x_2^2}{a_1^2} + \frac{x_2^2}{a_2^2} + \frac{(x_3 - c)^2}{a_3^2} \leq 1.$$

Applying transformations

$$x_1 = y_1, \quad x_2 = y_2, \quad x_3 = y_3 + c,$$

$$x'_1 = y'_1, \quad x'_2 = y'_2, \quad x'_3 = y'_3 + c,$$

and

$$x_1 = z_1, \quad x_2 = z_2, \quad x_3 = z_3 - c,$$

$$x'_1 = z'_1, \quad x'_2 = z'_2, \quad x'_3 = -z'_3 + c,$$

R_1 and R_2 can be expressed as:

$$R_1^2 = (y_1 - y'_1)^2 + (y_2 - y'_2)^2 + (y_3 - y'_3)^2,$$

$$R_2^2 = (z_1 - z'_1)^2 + (z_2 - z'_2)^2 + (z_3 - z'_3)^2.$$

The domain of integration changes to

$$\Omega_1 : \frac{y_1^2}{a_1^2} + \frac{y_2^2}{a_2^2} + \frac{y_3^2}{a_3^2} \leq 1,$$

for the integral involving R_1 , and to

$$\Omega_2 : \frac{z_1^2}{a_1^2} + \frac{z_2^2}{a_2^2} + \frac{z_3^2}{a_3^2} \leq 1,$$

for the integrals involving R_2 .

Dyson [33] expressed both Ψ^I and Ψ^{II} in the form:

$$\pi a_1 a_2 a_3 \int_{\lambda}^{\infty} \left[\frac{1}{2} \frac{d}{ds} \left(\frac{U^2 s^2}{\Delta} \right) - \frac{1}{4} \frac{U^2 s}{\Delta} \right] ds,$$

and both ϕ^I and ϕ^{II} in the form:

$$\pi a_1 a_2 a_3 \int_{\lambda}^{\infty} \frac{U}{\Delta} ds.$$

For the integrals involving R_1 , i.e. Ψ^I and ϕ^I ,

$$U = 1 - \left(\frac{y_1^2}{a_1^2 + s} + \frac{y_2^2}{a_2^2 + s} + \frac{y_3^2}{a_3^2 + s} \right),$$

$$\Delta = \{(a_1^2 + s) + (a_2^2 + s) + (a_3^2 + s)\}^{1/2},$$

and

$$\frac{y_1^2}{a_1^2 + \lambda} + \frac{y_2^2}{a_2^2 + \lambda} + \frac{y_3^2}{a_3^2 + \lambda} = 1,$$

($\lambda = 0$ for the interior and $\lambda \neq 0$ for the exterior of Ω_1).

For the integrals involving R_2 , i.e. Ψ^{II} and ϕ^{II} ,

$$U = 1 - \left(\frac{z_1^2}{a_1^2 + s} + \frac{z_2^2}{a_2^2 + s} + \frac{z_3^2}{a_3^2 + s} \right),$$

$$\Delta = \{(a_1^2 + s) + (a_2^2 + s) + (a_3^2 + s)\}^{1/2},$$

and

$$\frac{z_1^2}{a_1^2 + \lambda} + \frac{z_2^2}{a_2^2 + \lambda} + \frac{z_3^2}{a_3^2 + \lambda} = 1,$$

($\lambda = 0$ for the interior and $\lambda \neq 0$ for the exterior of Ω_2).

References

- [1] Gibson LJ, Ashby MF. Cellular solids: structure and properties. 2nd ed. New York: Cambridge University Press; 1997.
- [2] Ashby MF, Evans AG, Fleck NA, Gibson LJ, Hutchinson JW, Wadley HNG. Metal foams: a design guide. Boston, MA: Butterworth-Heinemann; 2000.
- [3] Oppenheimer S, Dunand DC. Acta Mater 2010;58:4387.
- [4] Banhart J, Fleck NA, Mortensen A. Cellular metals: manufacture, properties and application. Berlin: MIT-Verlag; 2003.
- [5] Ford CM, Gibson LJ. Int J Mech Sci 1998;40:521.
- [6] Kitazono K, Sato E, Kuribayashi K. Acta Mater 2003;51:4823.
- [7] Drenchev L, Sobczak J, Sobczak N, Sha W, Malinov S. Acta Mater 2007;55:6459.
- [8] Mori T, Tanaka K. Acta Metall 1973;21:571.
- [9] Benveniste Y. Mech Mater 1987;6:147.
- [10] Eshelby JD. Proc Roy Soc Lond A 1957;241:376.
- [11] Weng GJ. Int J Eng Sci 1984;22:845.
- [12] Tandon GP, Weng GJ. Comp Sci Technol 1986;27:111.
- [13] Zhao YH, Tandon GP, Weng GJ. Acta Mech 1989;76:105.
- [14] Dunn ML, Taya M. J Mater Sci 1994;29:2053.
- [15] Meraghni F, Blakeman CJ, Benzeggagh ML. Comp Sci Technol 1996;56:541.
- [16] Thevenin P, Perreux D. Comp Sci Technol 1996;56:595.
- [17] Dunn ML, Taya M. Int J Solids Struct 1993;30:161.
- [18] Gong S, Lia Z, Xu GY, Liu N, Zhao YY, Liang SQ. J Alloys Compd 2011;509:2924.
- [19] Lin SC, Mura T. Phys Status Solidi 1973;15:281.
- [20] Mindlin RD. Force at a point in the interior of a semi-infinite solid. Department of Civil Engineering; 1953.
- [21] Mura T. Micromechanics of defects in solids. 2nd ed. Dordrecht, The Netherlands: Martinus Nijhoff Publishers; 1982.
- [22] Zhao YY, Sun DX. Scripta Mater 2001;44:105.
- [23] Gong S, Xiao ZA, Li Z. Adv Mater Res 2010;123:1011.
- [24] Zhao YY, Han FS, Fung T. Mater Sci Eng A Struct Mater Prop Microstruct Proc 2004;364:117.
- [25] Zhao YY, Fung T, Zhang LP, Zhang FL. Scripta Mater 2005;52:295.
- [26] Sun DX, Zhao YY. Metall Mater Trans B 2003;34B:69.
- [27] El-Hadek MA, Kaytbay S. Int J Mech Mater Des 2008;4:63.
- [28] Zivcova Z, Cerny M, Pabst W, Gregorova E. J Eur Ceram Soc 2009;29:2765.
- [29] Mondal DP, Ramakrishnan N, Suresh KS, Das S. Scripta Mater 2007;57:929.
- [30] Hashin Z, Shtrikman S. J Mech Phys Solids 1963;11:127.
- [31] Lakes RS. J Mater Sci 1983;18:2572.
- [32] Brezny R, Green DJ. Acta Metal Mater 1990;38:2517.
- [33] Dyson FW. Quart J Pure Appl Math 1891;25:259.